Lin Cissi Y. (Orcid ID: 0000-0002-2071-1948)
Deng Yue (Orcid ID: 0000-0002-8508-1588)

Atmospheric Gravity Waves in the Ionosphere and Thermosphere During the 2017 Solar Eclipse

Cissi Y. Lin[1]

Yue Deng[1]

Aaron Ridley[2]

[1]Department of Physics, University of Texas at Arlington, Arlington, Texas, USA

[2]Department of Atmospheric, Oceanic, and Space Sciences, University of Michigan, Ann Arbor, Michigan, USA

Corresponding author: yuedeng@uta.edu

Abstract

As a cavity of solar radiation created by the lunar shadow moves across the United States on August 21, 2017, decreases in local ionospheric and thermospheric (IT) temperature and density are anticipated. The average velocity of the total solar eclipse across the United States is ~700 m/s. The supersonically-moving lunar shadow has induced bow waves and gravity waves that are observed by the GNSS network. We use the Global Ionosphere Thermosphere Model, a global circulation model solving for non-hydrostatic equations, with high-resolution (2° in longitude and 0.5° in latitude) and high-cadence (forcing updated every 2 seconds) settings to investigate the IT responses related to the atmospheric gravity wave perturbations during the solar eclipse. The modeled IT conditions extracted at 5-second cadence at two ground stations reveal different responses in both neutral and electron densities under totality and partial-eclipse scenarios. A bow wave of -0.2 TECu develops hours after the eclipse started, which is comparable with GNSS observations. Gravity waves with period of 20-30 minutes observed by GNSS have been reproduced in our simulations.

Plain Language Summary

Just as a boat moving through the surface of a lake stirs up waves in its wake, the lunar shadow moving across continents stirs up waves in our atmosphere during a solar eclipse. While the 2017 solar eclipse allowed a once-in-a-lifetime viewing opportunity for over 200 million Americans, it also allowed scientists to capture unambiguous bow waves predicted by theoretical studies decades ago with the modern Global Navigation Satellite System (GNSS). In this study, we use a self-consistent global circulation model for the upper atmosphere to further confirm the formation of bow waves by the supersonically moving lunar shadow. Waves with period of 20-30 minutes observed by GNSS have been reproduced in our simulations.

Keywords: solar eclipse, gravity waves, bow waves

Key Points

1. Supersonically moving lunar shadow induces mesoscale waves at totality locations.
2. A bow-wave front led by the lunar shadow is formed with modification of the in-situ forcing.
3. VTEC have strong wave responses with periods of 20–30 minutes.

1 Introduction

The atmospheric response during a solar eclipse has been observed [Altadill et al., 2001; Jakowski et al., 2008; MacPherson et al., 2000] and studied for decades [Chimonas, 1970; Chimonas and Hines, 1971; Fritts and Luo, 1993]. The path of the 2017 solar eclipse crossed fourteen U.S. states, entering Oregon and leaving South Carolina, on August 21, 2017. The long duration of its totality path on land (~2 hours) provided a unique opportunity for scientific exploration in the modern age. Thousands of GNSS receivers across the continental U.S observed the event [Coster et al., 2017; Zhang et al., 2017]. A wide community of ham radio operators participated in innovational experiments, HamSCI, to communicate using high frequency radios (1–30 MHz) during the day. The Super Dual Auroral Radar Network (SuperDARN), and scintillation receivers were coordinated to observe the event simultaneously.

Total electron content (TEC) derived from GNSS receivers have captured large-scale and medium-scale traveling disturbances (LSTIDs and MSTIDs) induced from various lower-atmospheric sources, including tsunamis [Galvan et al., 2011; Occhipinti et al., 2006; Saito et al., 2011; Tsugawa et al., 2011] and strong tropical systems in the troposphere [Nishioka et al., 2013; Perwitasari et al., 2015; Yue et al., 2014]. Theoretical works have used moving wave packets as forcing to drive lower and upper atmospheric models [Hickey et al., 2009; Meng et al., 2015; Vadas et al., 2015]. Depending on the propagation velocity, moving wave packets in the lower thermosphere induce acoustic or gravity waves. Upward propagating gravity waves result in perturbations observable in both neutral and electron densities. The induced perturbations in

TEC may be sustained tens of minutes to hours as gravity waves after the lower boundary wave packet has passed. The effects of acoustic waves, however, are more transient and localized to the atmosphere encountering the wave packet than the effects of induced gravity waves [Lin et al., 2017].

Gravity waves observed in the upper atmosphere are primarily induced by 1) waves propagating from the lower atmosphere and 2) in-situ modification to energy, chemistry, or dynamics. The reduction of heating sources (e.g. ozone at 45 km or EUV heating above 100 km) in the atmosphere can become a source for generating atmospheric perturbations. Theoretical calculation [Chimonas, 1970; Chimonas and Hines, 1971; Fritts and Luo, 1993] has shown that such a source moving at supersonic speeds is expected to induce a bow wave and acoustic gravity waves in the lower atmosphere and may be observed in the form of TIDs in the upper atmosphere. Global 3D simulations have been performed to study the effects of a solar eclipse on the terrestrial atmosphere up to the altitude of ~80 km [Eckermann et al., 2007]. In the study, the reduced ozone heating resulted in a distinguishable bow wave observed in geopotential height at a pressure of 0.01 hPa approximately 4 hours after the eclipse started. Owing to the limit of the model employed, the heating and cooling parameterization was not valid above 0.01 hPa. The results from a coarse-resolution global simulation of the upper atmosphere suggested that a solar eclipse may drive large-scale (greater than 1000 km) wave-like features in temperature and neutral wind changes [Müller-Wodarg et al., 1998]. The lunar shadow moved supersonically on Aug 21, 2017: averaging roughly 700 m/s [Huba and Doug, 2017], or about 1000 m/s in Oregon and slowing to about 650 m/s in South Carolina [Coster et al., 2017]. For the first time, the dense GNSS network provided measurements an unambiguous bow wave during the August 21 eclipse [Zhang et al., 2017]. Mesoscale wave structures with a period of 25 minutes were observed, which agree with the prediction of a dominant wave period of ~20 minutes at an altitude of 300 km [Chimonas and Hines, 1971]. In this study, the mesoscale features that may have been induced by the 2017 eclipse are presented. The Global Ionosphere-Thermosphere Model (GITM) is used to study aspects of the effect of the eclipse on the upper atmosphere that have not been studied previously.

2 Methodology

GITM is a self-consistent 3D ionosphere-thermosphere model [Ridley et al., 2006] with the advantages of flexible 3D grid sizes and the ability to solve for non-hydrostatic solutions [Deng et al., 2008]. For this study, we performed global simulations with the resolution of 2° by 0.5° in latitude and longitude, which is roughly equivalent to a resolution of 150 km by 50 km at the U.S. sector. The resolvable horizontal wavelength in the diagonal direction is 316 km. The altitudinal range extended from 100 to ~700 km with a vertical resolution of roughly one third of the scale height. The time-step was roughly 2s, which was needed in order to capture both the acoustic waves and normally strong ion flows at high latitudes. The simulations started at 13:30 UT on Auguest 20, 2017 and ended at 23:30 UT on August 21, 2017. The first 24 hours were used to spin up the codes.

While the visible light is completely blocked by the lunar body during totality, the EUV radiation from the corona does not reduce completely, resulting in weakened but non-zero ionization and heating in the upper atmosphere. Marriott et al. [1971] considered the ratio of electron production rate during an eclipse to that on a regular day as the *obscuration factor*. Adopting the idea, Huba and Drob [2017] used solar images to predict the obscuration factor during the 2017 eclipse and applied the factor to the amount of EUV flux within the radius of the eclipsed atmosphere by the lunar shadow. In this study, the scaling factor is considered as 10% at totality, linearly increasing toward the edge of the impacted area at a radius of approximately 3000 km, and returning to 100% outside of the linear region with a smooth transition of a quarter sinusoidal function. Without considering the actual features on the solar disk, it implies a uniform EUV flux distribution and this factor is simply a function of radius of the shadow. The left panel of Figure 1 illustrates the temporal variation of the scaling factor for totality (blue) and partial-eclipse (orange) scenarios. This implementation allows effective calculation at each 2-second time step in the GITM simulation and facilitate the establishment a baseline for investigating high-frequency mesoscale perturbations caused by the eclipse.

Two separate simulations are performed: a control run and an eclipse run with the temporally and spatially varying scaling factor. The differences between the control run and the eclipse run are considered as consequential atmospheric responses to the eclipse. Particularly, thermospheric and ionospheric variables at two ground stations are extracted from the 3D simulation. The stations are located in Missouri (MO, 39°N, 93°W) and Massachusetts (MA, 42.6°N, 71.5°W), where GNSS TEC or incoherent scatter radar measurements were taken. The MO station experienced totality while the maximal obscuration at the MA station was 63%. The time for maximal obscuration at the two stations was 18:13 UT (13:13 CDT) and 18:46 UT (14:46 EDT) respectively.

3 Results

One-dimensional column values were extracted from the global 3D simulation results at the two locations from about 3 hours before and 2 hours after totality. Figure 2 shows the differential fields of neutral mass density (left column) and electron number density (right column) at the two ground stations: (top) MO; and (bottom) MA. The large-scale IT responses at the two stations were similar but different in several fashions. The electron density showed similar trends at both stations. The maximal decrease below ~200 km occurs during maximal obscuration, marked by the black vertical line. The loss of solar EUV radiation resulted in a rapid decrease in the electron density in the E region as it is the main ionization source there. Transport contributes significantly to the electron density balance at the higher altitudes, where the maximal decrease occurs about 30 minutes later. The temperature decrease in the lower thermosphere, resulting from reduced EUV heating, peaked at 200 km and reached its minima of -41K and -42 K, at the MO and MA stations respectively ~30 minutes after maximal obscuration (not shown). Consequentially, the neutral density decreased by 25% at both stations. Wave activity in both mass density and electron density is clearly observable at the MO station as shown in Figures 2(a, b). High-frequency waves are induced when local obscuration started and became more significant after the totality epoch as indicated by the vertical black line. However, wave activity is significantly diminished at the MA station. The different responses observed at the stations (totality versus partial eclipse) may possibly be attributed to the change rate of the EUV scaling factor (greater versus smaller gradient). Particularly, the sharp transition before and after totality when the signs of the change rate flip imposes a *wave-like* forcing to the atmosphere. The right panel of Figure 1 shows that the change rate changes from negative to positive as the lunar shadow comes toward and then goes away from the observer. The piecewise change rate can be linearly approximated by three straight lines, marking the middle section the *transition*. Where the transition intersects with the other two lines at either sides determines the transition duration. As at a totality location the transition takes less than 3 minutes, oscillations of periods of a few minutes are likely to be induced. At the partial-eclipse stations, the geometry determines the duration of the transition: a shorter (longer) period of transition and a higher (lower) slope when being closer to (farther away from) the totality path. In the case of the MA station, the transition takes about 30 minutes at the maximal EUV obscuration and hypothetically is likely to induce oscillations of period of 10s minutes to an hour.

Figure 3 shows the logarithmic fast Fourier transform (FFT) power spectrum for each percentage-differential field shown in Figure 2. A strong wave-like component of periods of 40–50 minutes was observable at and above 300 km in neutral density at both stations in Figures 3(a, c). The short-period waves with periods of 5–15 min minutes with similar strengths as the 40–50 minute components were only observed at the totality station (MO) above 200 km but absent from the partial-eclipse station (MA). On the other hand, Figures 3(b, d) show that the waves in electron density at the totality station are strongest below 300 km. Similar to the neutral density, wave components of 5–15 minutes in electron density were observed only above 300 km at the MO station but less distinct at the MA station. Cautions have to be taken when interpreting the longer-period wave-like components in Figure 3. They merely represent the large-scale density depletion by the eclipse, which last about 1–2 hours as shown in Figure 2.

As waves develop in the electron density through all of the altitudes, it is expected that such wave signatures would also appear in the vertical total electron content (VTEC). Electron density is height-integrated up to ~450 km from the simulation results. To separate mesoscale variability from the large-scale background depletion (~-2 TECu at maximal obscuration), a three-degree zero-order Savitzky-Golay filter of 8˚ in longitude/latitude was applied to the global VTEC at fixed latitudes/longitudes respectively. Figure 4 shows the de-trended results. At 18:30 UT, lunar shadow moves to around (36°N, 272°E) marked by the hollow white circle. A bow wave front had been formed by this time. As electron density grows with altitude, electron density at higher altitudes dominates the overall wave signatures observed in our results (Figure 4).

In previous studies of the lower atmosphere [Eckermann et al., 2007], weaken ozone heating was attributed to be the main source of the waves induced during a solar eclipse. One of the advantages of simulating the solar eclipse event is that it was possible to distinctly investigate if in-situ forcing in the upper atmosphere contributed to the observed bow waves and gravity waves in TEC. Figure 4(a) shows that a bow wave front can be formed with only the in-situ modification to the forcing and without a lower-atmospheric source. The bow wave front led by the lunar shadow had a magnitude of -0.2 TECu, which agrees well with the magnitude reported in Zhang et al. [2017]. The quadrangular white area in (a) indicates perturbation magnitude exceeding 0.2 TECu. The high-resolution and high-cadence GITM outputs also allowed the extraction of high-frequency wave components that were close to the local buoyancy frequency. From west to east, two crosses in Figure 4(a) mark the locations of the MO and MA stations. A three-degree zero-order Savitzky-Golay filter of 60 minutes was applied to the VTEC at these locations. Figures 4(b, c) show the FFT power spectra of the de-trended VTEC perturbations at the two stations. The de-trended VTEC displays significant wave activity lasting at least 2 hours at the totality station since the passing of the lunar shadow. While no clear waves were detected at the MA station, wave components of periods of 10–40 minutes were most prominent at the MO station. Especially, the 20–30 minute waves dominate the spectra, which agrees well with the wave periods of mesoscale gravity waves extracted from the GNSS observations during the 2017 eclipse [Zhang et al., 2017] as well as the theoretical predictions by Chimonas and Hines [1971].

The trailing gravity waves close to the MO station in our simulations showed an eastward propagation speed of 155 m/s and a southward propagation speed of 200 m/s. The waves lasted at least one hour since the local totality. Given the grid resolutions in this simulation is 2˚x0.5˚ in longitude and latitude, which is roughly equivalent to a resolution of 150 km x 50 km in the U.S. sector. The resolvable horizontal wavelength in the diagonal direction is 316 km. The bow wavelengths reported by Zhang et al. [2017] is 350/270 km in the zonal/meridional direction, equivalent to a horizontal wavelength of 442 km. However, the aspect ratio of the GITM grids is different from the one employed by Zhang et al. [2017]. A projection at an angle of 19.3° between the two orientations therefore needs to be considered. Potentially, the projected wavelength of 417 km from Zhang et al. [2017] should be resolvable by the current simulation setting.

The de-trending processes in this study, however, were selected to best applicable to the nature of the data sets of interest and do not exactly resemble the process taken by Zhang et al. [2017], in which a low-pass filter was applied to each line-of-sight TEC profile from the GNSS satellites and the residual are binned to the 2D plane. However, comparing the contour in Figure 4(a) (the 2D GITM results) to Figure 2 in Zhang et al. [2017] and comparing the wave characteristics to the ones reported by the group provide a sufficient evidence to conclude that bow waves of similar characteristics are reproduced in the model given the limitation of different approaches. This may not, however, conclusively show the waves presented in this work are the exactly same modes of waves as those presented in Zhang et al. [2017]. Caution has to be taken when making a direct comparison between our simulation results and observations. The study by Mrak et al. [2017] have shown that the obscuration of an unevenly distribution EUV flux (two active regions present) from the solar atmosphere on Aug 21, 2017 might have imposed wave-like features with an amplitude of ~±0.2 TECu to the observed TEC perturbations. Nevertheless, the results in this study demonstrate that the bow waves can be triggered by a solar eclipse with uniformly distributed EUV flux across the solar disk and are likely a subset of waves observed by the GNSS network even without the inclusion of the consequential temporal evolution of the EUV flux related to its spatial distribution across the solar atmosphere.

4 Summary

In this study, GITM was used to simulate the 2017 solar eclipse event with high-resolution and high-cadence outputs. Strong high-frequency mesoscale wave activity was observable in both neutral and electron density at the totality station but absent from the partial-eclipse station. Particularly, the high-frequency wave components (periods of <15 minutes) observed in neutral density were as strong as the lower-frequency components (periods of ~60 minutes) at the totality station. The different responses observed at the totality and partial-eclipse stations are attributed to the rate of change of the EUV scaling factor. Strong wave activity in electron density contribute to the VTEC perturbations at the totality station, with the strongest waves having periods of 20–30 minutes lasting at least two hours since totality. The de-trended VTEC revealed a bow wave front led by the lunar shadow. The perturbation magnitude of -0.2 TECu associated with 20-30 minute waves agrees well with the characteristics observed by the GNSS network. Using GITM, we were able to confirm the generation of observable bow waves and gravity waves by differential in-situ heating during a solar eclipse.

Acknowledgement

This research at the University of Texas at Arlington was supported by NSF through grant ATM0955629, NASA through grants NNX13AD64G and NNX14AD46G, and AFOSR through award FA9550-16-1-0059 and MURI FA9559-16-1-0364. The authors acknowledge the Texas Advanced Computing Center (TACC) at the University of Texas at Austin for providing Lonestar5 and Maverick resources that have contributed to the research results reported within this paper. URL: http://www.tacc.utexas.edu. The GITM model outputs are available at https://github.com/cissilin/Lin2018GRL_SolarEclipse.

References

Altadill, D., J. G. Solé, and E. M. Apostolov (2001), Vertical structure of a gravity wave like oscillation in the ionosphere generated by the solar eclipse of August 11, 1999, J. Geophys. Res., 106(A10), 21419–21428, doi:10.1029/2001JA900069

Chimonas, G. (1970), Internal gravity-wave motions induced in the Earth's atmosphere by a solar eclipse, J. Geophys. Res., 75(28), 5545–5551, doi:10.1029/JA075i028p05545

Chimonas, G., and C. O. Hines (1971), Atmospheric gravity waves induced by a solar eclipse, 2, J. Geophys. Res., 76(28), 7003–7005, doi:10.1029/JA076i028p07003

Coster, A. J., Goncharenko, L., Zhang, S.-R., Erickson, P. J., Rideout, W., & Vierinen, J. (2017). GNSS observations of ionospheric variations during the 21 August 2017 solar eclipse, Geophys. Res. Lett, 44(24), 12041–12048, doi:10.1002/2017GL075774

Deng, Y., A. D. Richmond, A. J. Ridley and H.-L. Liu (2008), Assessment of the non-hydrostatic effect on the upper atmosphere using a general circulation model (GCM), Geophys. Res. Lett, 35, L01104, doi:10.1029/2007GL032182

Deng Y., A. Ridley (2014), Simulation of non-hydrostatic gravity wave propagation in the upper atmosphere, Ann. Geophys., 32, 443-447, doi:10.5194/angeo-32-443-2014

Eckermann, S. D., D. Broutman, M. T. Stollberg, J. Ma, J. P. McCormack, and T. F. Hogan (2007), Atmospheric effects of the total solar eclipse of 4 December 2002 simulated with a high-altitude global model, J. Geophys. Res., 112, D14105, doi:10.1029/2006JD007880

Fritts, D. C., and Z. Luo (1993), Gravity wave forcing in the middle atmosphere due to reduced ozone heating during a solar eclipse, J. Geophys. Res., 98(D2), 3011–3021, doi:10.1029/92JD02391

Galvan, D. A., A. Komjathy, M. P. Hickey, and A. J. Mannucci (2011), The 2009 Samoa and 2010 Chile tsunamis as observed in the ionosphere using GPS total electron content, J. Geophys. Res., 116, A06318, doi:10.1029/2010JA016204

Hickey, M. P., G. Schubert, and R. L. Walterscheid (2009), Propagation of tsunami-driven gravity waves into the thermosphere and ionosphere, J. Geophys. Res., 114, A08304, doi:10.1029/2009JA014105

Huba, J. D., and D. Drob (2017), SAMI3 prediction of the impact of the 21 August 2017 total solar eclipse on the ionosphere/plasmasphere system, Geophys. Res. Lett., 44, 5928–5935, doi:10.1002/2017GL073549

Jakowski, N. et al. (2008), Ionospheric behavior over Europe during the solar eclipse of 3 October 2005, J Atmos. Solar-Terres Phys., 70(6), 836–853, doi:10.1016/j.jastp.2007.02.016

Lin, C. Y., Y. Deng, C. Sheng, and D. P. Drob (2017), A study of the nonlinear response of the upper atmosphere to episodic and stochastic acoustic-gravity wave forcing, J. Geophys. Res. Space Physics, 122, 1178–1198, doi:10.1002/2016JA022930

Marriott, R. T., D. E. St. John, R. M. Thorne, and S. V. Venkateswaran (1971), XUV image of the sun from eclipse observations of the ionospheric E-region, Solar Phys., 21(2), 483–494, doi:10.1007/BF00154303

MacPherson, B., S. A. González, M. P. Sulzer, G. J. Bailey, F. Djuth, and P. Rodriguez (2000), Measurements of the topside ionosphere over Arecibo during the total solar eclipse of February 26, 1998, J. Geophys. Res., 105(A10), 23055–23067, doi:10.1029/2000JA000145

Meng, X., A. Komjathy, O. P. Verkhoglyadova, Y.-M. Yang, Y. Deng, and A. J. Mannucci (2015), A new physics-based modeling approach for tsunami-ionosphere coupling. Geophys. Res. Lett., 42, 4736–4744. doi:10.1002/2015GL064610

Mrak, Sebastijan, J. Semeter, D. Drob, and J. B. Huba (2017), Direct EUV/X-ray 213 modulation of the ionosphere during the Aug-21, 2017 total solar eclipse, doi:10.13140/RG.2.2.33100.10882.

Müller-Wodarg, I. C. F., A. D. Aylward, and M. Lockwood (1998), Effects of a mid-latitude solar eclipse on the thermosphere and ionosphere - A modelling study, Geophys. Res. Lett., 25(20), 3787–3790, doi:10.1029/1998GL900045

Nishioka, M., T. Tsugawa, M. Kubota, and M. Ishii (2013), Concentric waves and short-period oscillations observed in the ionosphere after the 2013 Moore EF5 tornado, Geophys. Res. Lett., 40, 5581–5586, doi:10.1002/2013GL057963

Occhipinti, G., P. Lognonne´, E. A. Kherani, and H. He´bert (2006), Three-dimensional waveform modeling of ionospheric signature induced by the 2004 Sumatra tsunami, Geophys. Res. Lett., 33, L20104, doi:10.1029/2006GL026865

Perwitasari, S., T. Sakanoi, A. Yamazaki, Y. Otsuka, Y. Hozumi, Y. Akiya, A. Saito, K. Shiokawa, and S. Kawamura (2015), Coordinated airglow observations between IMAP/VISI and a ground-based all-sky imager on concentric gravity wave in the mesopause, J. Geophys. Res. Space Physics, 120, 9706–9721, doi:10.1002/2015JA021424

Ridley, A. J., Y. Deng, and G. Tóth (2006), The global ionosphere-thermosphere model, J Atmos. Solar-Terres Phys., 68(8), 839–864, doi:10.1016/j.jastp.2006.01.008

Saito, T., Y. Ito, D. Inazu, and R. Hino (2011), Tsunami source of the 2011 Tohoku-Oki earthquake, Japan: Inversion analysis based on dispersive tsunami simulations, Geophys. Res. Lett., 38, L00G19, doi:10.1029/2011GL049089

Savitzky, A., and Golay, M. J. E. (1964), Smoothing and differentiation bysimplifiedleastsquares procedures, Analytical Chemistry, 36, 1627–1639, doi:10.1021/ac60214a047

Tsugawa T., A. Saito, Y. Otsuka, M. Nishioka, T. Maruyama, H. Kato, T. Nagatsuma, and K. T. Murata, Ionospheric disturbances detected by GPS total electron content observation after the 2011 off the Pacific coast of Tohoku Earthquake, Earth Planets Space, 63, 875–879, doi:10.5047/eps.2011.06.035

Vadas, S. L., J. J. Makela, M. J. Nicolls, and R. F. Milliff (2015), Excitation of gravity waves by ocean surface wave packets: Upward propagation and reconstruction of the thermospheric gravity wave field, J. Geophys. Res. Space Physics, 120, 9748–9780, doi:10.1002/2015JA021430

Yue, J., B. Thurairajah, L. Hoffmann, J. Alexander, A. Chandran, M. J. Taylor, J. M. Russell III, C. E. Randall, and S. M. Bailey (2014), Concentric gravity waves in polar mesospheric clouds from the Cloud Imaging and Particle Size experiment, J. Geophys. Res. Atmos., 119, 5115–5127, doi:10.1002/2013JD021385

Zhang, S.-R., Erickson, P. J., Goncharenko, L. P., Coster, A. J., Rideout, W., & Vierinen, J. (2017). Ionospheric bow waves and perturbations induced by the 21 August 2017 solar eclipse, Geophys. Res. Lett, 44(24), 12067–12073, doi:10.1002/2017GL076054

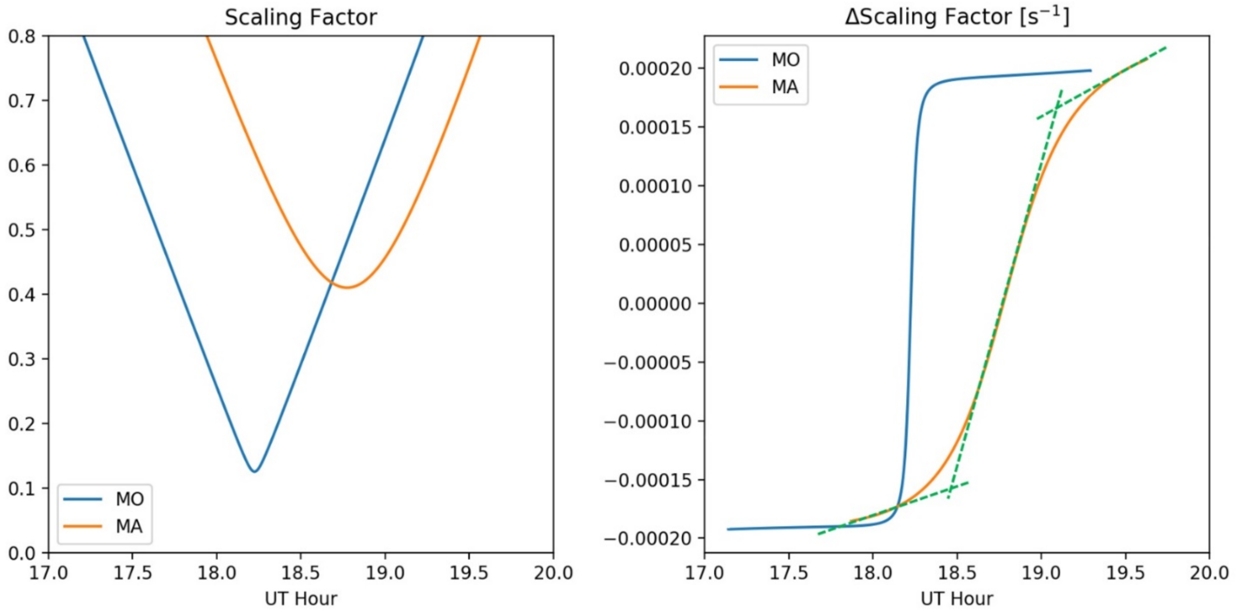

Figure 1. (Left) Temporal variation of the EUV scaling factor at the MO and MA stations. (Right) Change rate of the scaling factor at the two stations. The green dashed lines illustrate the estimation of the transition, defined by the linear approximation of the piecewise change rates.

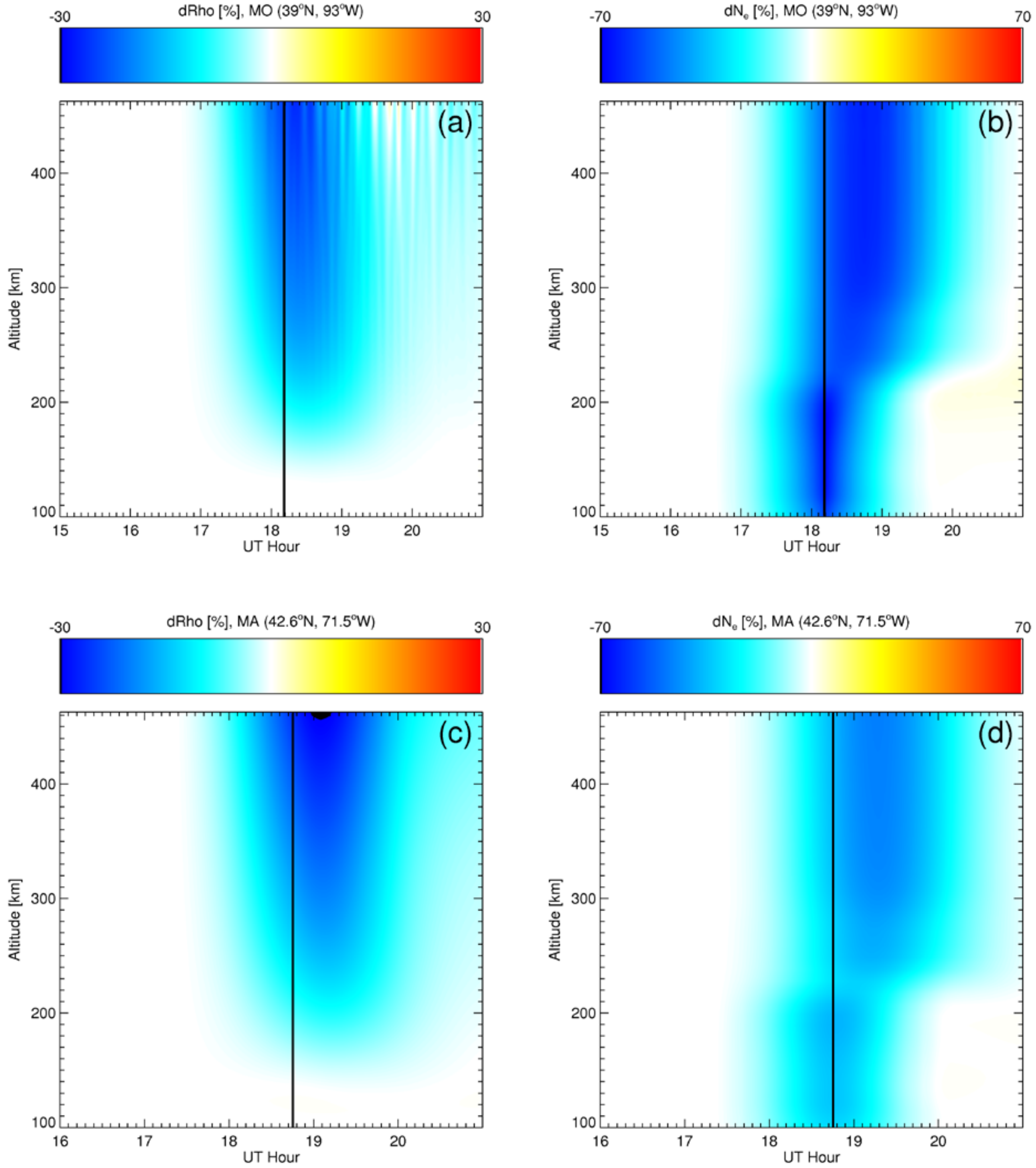

Figure 2. Differential fields of (a, c) neutral mass density and (b, d) electron density observable from the MO station undergoing totality (top row) and the MA station, where the maximal

obscuration is 63% (bottom row). The maximal obscuration at each location is marked by a vertical black line.

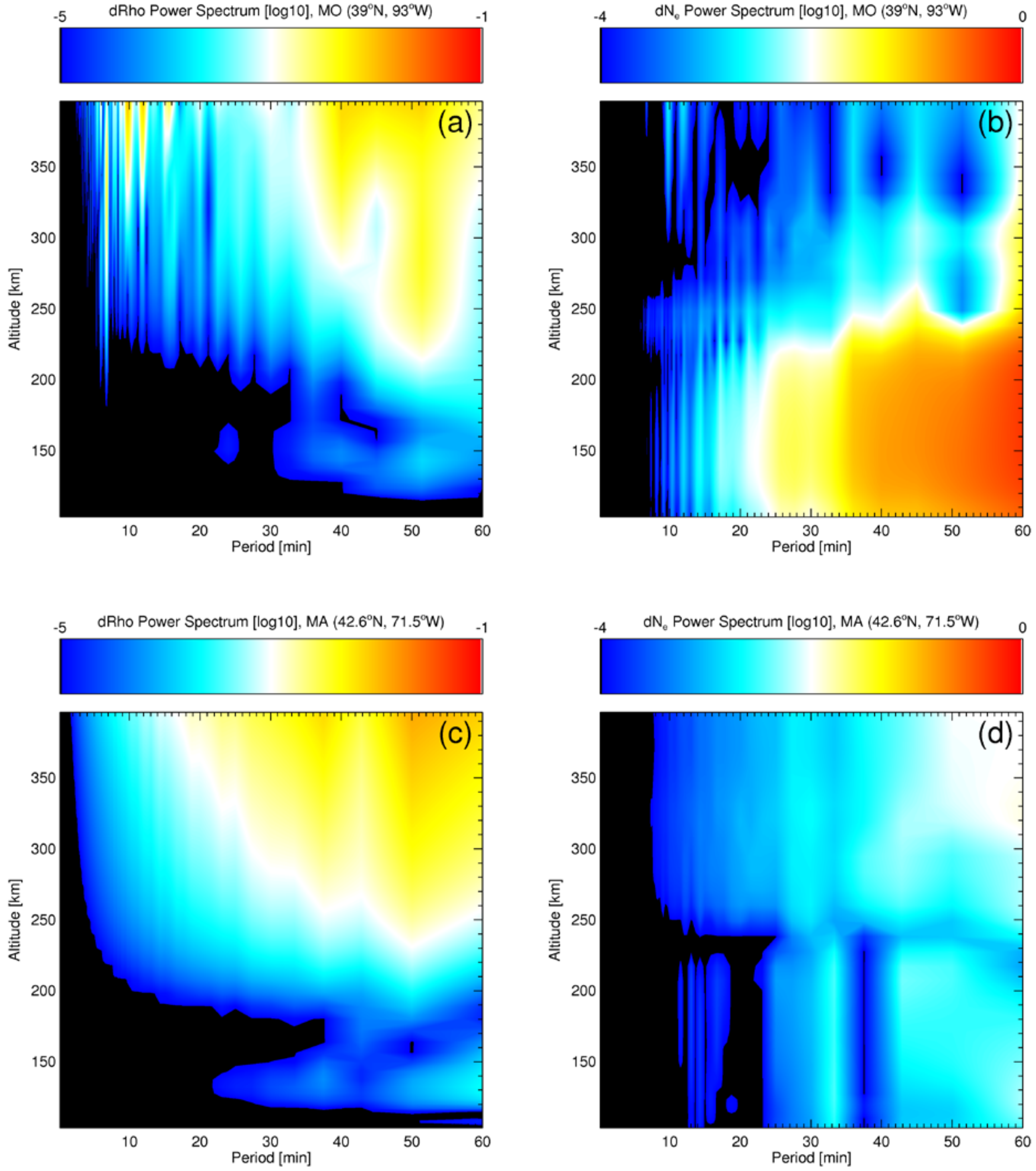
dRho Power Spectrum [log10], MO (39°N, 93°W)
-5
-1
(a)
Altitude [km]
Period [min]
dN$_e$ Power Spectrum [log10], MO (39°N, 93°W)
-4
0
(b)
dRho Power Spectrum [log10], MA (42.6°N, 71.5°W)
-5
-1
(c)
dN$_e$ Power Spectrum [log10], MA (42.6°N, 71.5°W)
-4
0
(d)
150
200
250
300
350
10
20
30
40
50
60

Figure 3. Periodogram of the corresponding (a, c) thermospheric and (b, d) ionospheric oscillation observable from the two stations. The panels are orientated similarly to the ones in Figure 1.

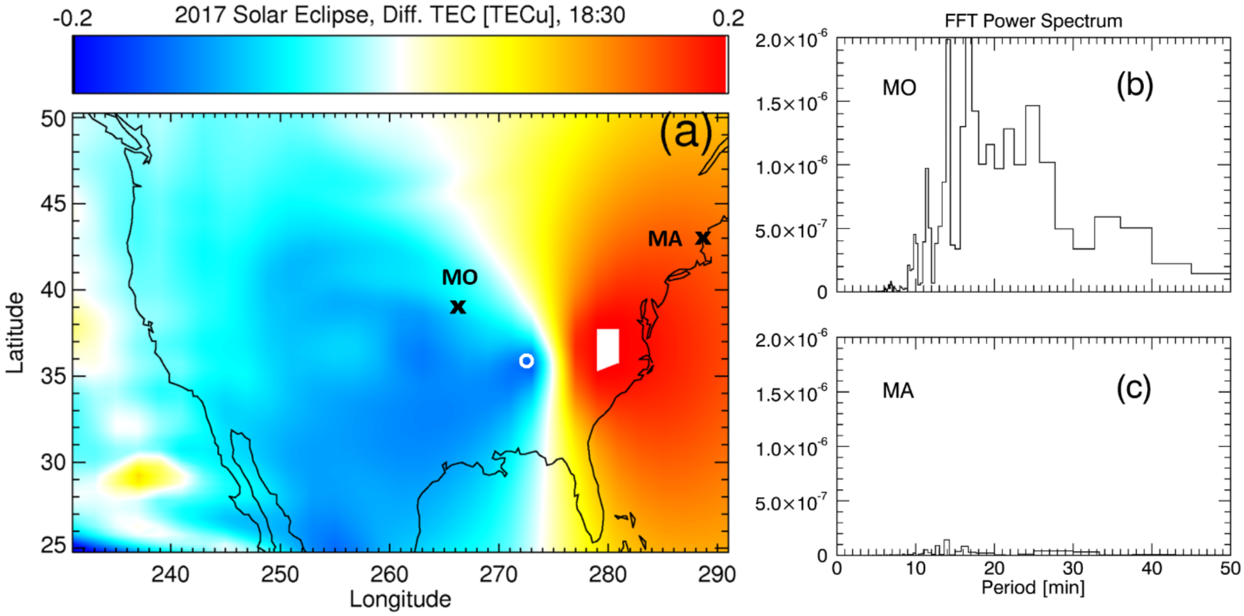

Figure 4. De-trended observable TEC perturbations. (a) A clear bow wave front formed as the eclipse moves across the U.S. and the crosses from west to east mark the (b) MO and (c) MA stations, where the FFT power spectra are derived from the high-cadence VTEC output. The lunar shadow is marked by the hollow white circle. The quadrangular white area in (a) indicates perturbation magnitude exceeding 0.2 TECu.